Heliyon 10 (2024) e23558

Contents lists available at ScienceDirect

Heliyon

journal homepage: www.cell.com/heliyon

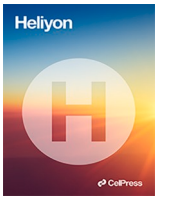

3D reconstruction of the uterus and automatic segmentation of the uterine cavity on 3D magnetic resonance imaging: A preliminary study

Qing Zhou [a,1], Yunhao Bai [b,1], Fang Chen [c,1], He Zhang [a], Limei Chen [c], Guofu Zhang [a,***], Yan Wang [b,**], Long Sui [c,*]

[a] Department of Radiology, Obstetrics and Gynecology Hospital of Fudan University, Shanghai, 200011, China
[b] Shanghai Key Laboratory of Multidimensional Information Processing, East China Normal University, Shanghai, 200241, China
[c] Cervical Center, Obstetrics and Gynecology Hospital of Fudan University, Shanghai, 200011, China

ARTICLE INFO

Keywords:
Deep learning
Magnetic resonance imaging
Septate uterus
3D reconstruction
Automatic segmentation

ABSTRACT

Purpose: To determine the differences in 3D shape features between septate uterus (SU) and normal uterus and to train a network to automatically delineate uterine cavity on 3D magnetic resonance imaging (MRI).

Methods: A total of 43 patients (22 cases of partial septate uterus and 21 cases of complete septate uterus) were included in the experimental group. Nine volunteers were recruited as a control group. The uterine cavity (UC), myometrium (UM), and cervical canal of the uterus were segmented manually using ITK-SNAP software. The three-dimensional shape features of the UC and UM were extracted by using *PyRadiomics*. The recurrent saliency transformation network (RSTN) method was used to segment the UC.

Results: The values of four 3D shape features were significantly lower in the control group than in the partial septate group and the complete septate group, while the values of two features were significantly higher ($p < 0.05$). The UCs of the three groups were significantly different in terms of flatness and sphericity. The values of six features were significantly lower in the UMs of the control group than in those of the partial septate group and the complete septate group ($p < 0.05$). After the deep learning networks were trained, the Dice similarity coefficient (DSC) scores of the four folds for different thresholds were all over 80 %. The average volume ratio between predictions and manual segmentation was 101.2 %.

Conclusions: Based on 3D reconstruction, 3D shape features can be used to comprehensively evaluate septate uterus and provide a reference for subsequent research. The UC can be automatically segmented on 3D MRI using the RSTN method.

* Corresponding author. Cervical Center, Obstetrics and Gynecology Hospital of Fudan University, No.419 Fangxie Road, Shanghai 200011, China.
** Corresponding author. Shanghai Key Laboratory of Multidimensional Information Processing, East China Normal University, No. 500 Dongchuan Road, Shanghai 200241, China.
*** Corresponding author. Department of Radiology, Obstetrics & Gynecology Hospital of Fudan University, No.419 Fangxie Road, Shanghai 200011, China.
E-mail addresses: guofuzh@fudan.edu.cn (G. Zhang), ywang@cee.ecnu.edu.cn (Y. Wang), suilong@fudan.edu.cn (L. Sui).
[1] Authors contributed equally to this work.

https://doi.org/10.1016/j.heliyon.2023.e23558
Received 20 January 2023; Received in revised form 2 December 2023; Accepted 6 December 2023
Available online 10 December 2023

1. Introduction

Septate uterus (SU) is a common congenital uterine malformation, accounting for approximately 80 %–90 % of all Mullerian duct anomalies (MDAs) [1]. The mediastinum of the uterus can change the morphology of the uterine cavity, leading to female infertility, recurrent pregnancy loss, premature birth, stillbirth, and other adverse pregnancy outcomes [2,3]. Surgical metroplasty has been shown to improve outcomes in these cases, and preoperative planning is critical [4–8]. Therefore, it is paramount to fully understand the 3D structure of the malformed uterus and accurately evaluate the morphology of the uterine cavity before surgical metroplasty. Ultrasonography (US) is the first-line method for diagnosing SU because it is readily available, inexpensive, and rapid and does not use ionizing radiation. Although 3D US may improve assessment of the external uterine contour compared with 2D imaging, a confident diagnosis is frequently difficult [4]. Magnetic resonance imaging (MRI) is the imaging standard of reference; it is noninvasive, does not involve ionizing radiation, has multiplanar capabilities, allows excellent soft-tissue characterization, and can image a wider field of US [9,10]. 3D-T2WI of the pelvis allows multiplanar reformatting (MPR) of the uterus, aiding in the characterization of the anomaly. Reconstruction of the 3D image is a good reference for preoperative planning. Based on the original 2D images, the radiologist can outline the morphology of the cavity slice by slice and then obtain 3D reconstruction images with internal software. However, this procedure is tedious, time consuming, and operator dependent; for these reasons, it is not routinely performed in clinical practice.

Abbreviations

SU	septate uterus
MRI	magnetic resonance imaging
UC	uterine cavity
UM	myometrium
RSTN	recurrent saliency transformation network
DSC	Dice similarity coefficient
MDAs	Mullerian duct anomalies
US	Ultrasonography
MPR	multiplanar reformatting
TCIS	transcervical incision of the septum
TR/TE	repetition time/echo time

In recent years, machine learning technology has been blooming, and its application has gradually increased in clinical medicine as a tool to help with laborious tasks, a role in which it has achieved promising results. However, similar studies on the automatic recognition of uterine cavity morphology are still very limited. Here, we use the recurrent saliency transformation network (RSTN) method, which was primarily proposed for the segmentation of very small targets [11]. The RSTN method adopts a coarse-to-fine segmentation strategy, which achieves good segmentation even with small targets and fits the structure of septate uteruses well.

To our knowledge, we are first to analyze the morphology of SU through 3D reconstruction. Based on this preliminary study, we sought to obtain a quantitative index or marker to evaluate the effect of the uterine mediastinum on fertility and evaluate the necessity and prognosis of surgery through big-data research on septate uterine segmentation in the future.

The purpose of this study was twofold: (1) to determine the difference in 3D shape features between SU and normal uterus and (2) to train a network to automatically delineate the uterine cavity (UC) on 3D MRI.

2. Materials and methods

2.1. Patients

A retrospective analysis of 43 patients who underwent transcervical incision of the septum (TCIS) in the Cervical Disease Clinic of our institution from January 2019 to December 2021 for septate uterus (22 cases of partial septate uterus and 21 cases of complete septate uterus) was performed. Patients with MRI examination data were selected as the experimental group and then divided into the partial septate group and the complete septate group. Nine women of normal reproductive age (both fertile and nulliparous) were recruited to volunteer as a control group. Every patient and control participant underwent MRI examination one week before menstruation, during which the endometrium is thicker than at other times, making it easier to observe the shape of the UC.

Cases were selected through TCIS results, laboratory results, and imaging results during follow-up.

Inclusion criteria: female patients of childbearing age, over 18 and under 50 years old; normal hormone levels (including follicle-stimulating hormone, luteinizing hormone, estradiol, progesterone, testosterone, prolactin, tested on the 3rd to 5th day of menstruation); normal ovulation (a large mature follicle or corpus luteum was observed on the ovary by ultrasound); ultrasound or MRI exclusion of complications that may affect uterine morphology and lead to infertility, such as uterine fibroids, uterine adenomyosis, fluid accumulation in the UC, ovarian cysts and uterine adhesions; and no serious systemic diseases such as hypertension, diabetes, and nephrotic syndrome.

The present study protocol was reviewed and approved by the Institutional Review Board of Obstetrics and Gynecology Hospital of

Fudan University (approval No. 2022-77). Informed consent was obtained for the control group (normal uterus) and the experimental group (septate uterus).

2.2. Image acquisition

MR examination was performed using a 1.5-T MR unit (Magnetom Avanto, Siemens) with a phased-array coil. During scanning, the patient lay supine and breathed calmly. The 3D T2WI SPACE sequence was used for the MRI evaluation. The acquisition parameters were as follows: repetition time/echo time [TR/TE], 2000/126 msec; slice thickness, 1 mm; matrix size, 256 × 256 or 320 × 320; flip angle, 150 deg; voxel size, 1 × 1 × 1 mm; and bandwidth, 651 Hz/pixel.

2.3. Segmentation and 3D shape feature extraction

The UC, myometrium, and cervical canal were segmented manually using ITK-SNAP software. 3D images were reconstructed based on 2D segmentation data, as shown in Fig. 1.

3D shape features were extracted by using the open-source Python package *PyRadiomics* (https://pypi. org/project/pyradiomics/). Before feature extraction, the intensity values were normalized, and the gray-level intensities in the images were distributed in the range of 0–600. The following 14 3D shape features of the UC and UM were extracted: Elongation, Flatness, LeastAxisLength, MajorAxisLength, Maximum2DDiameterColumn, Maximum2DDiameterRow, Maximum2DDiameterSlice, Maximum3DDiameter, MeshVolume, MinorAxisLength, Sphericity, SurfaceArea, SurfaceVolumeRatio, VoxelVolume.

The unpaired *t*-test was performed to compare normally distributed continuous variables between groups. A *P* value of less than 0.05 indicated statistical significance. SPSS (SPSS Inc., version 25.0) was used to perform all statistical analyses.

2.4. Automatic segmentation

We first obtained 44 3D MRI images (35 from the experimental group and 9 from the control group) and corresponding annotations with shapes of (256, 256, L) or (320, 320, L), where L ranged from 36 to 104. We performed standard cross-validation, dividing all samples into four folds of 11 cases each. We used 3 out of 4 folds (i.e., 33 samples) for training and then tested the model on the remaining fold (i.e., 11 samples).

2.4.1. Notations

Let a scanned 3D image be a volume denoted by **X**, which has a size of $W \times H \times L$. In our MRI dataset, W and H are 256 or 320, and

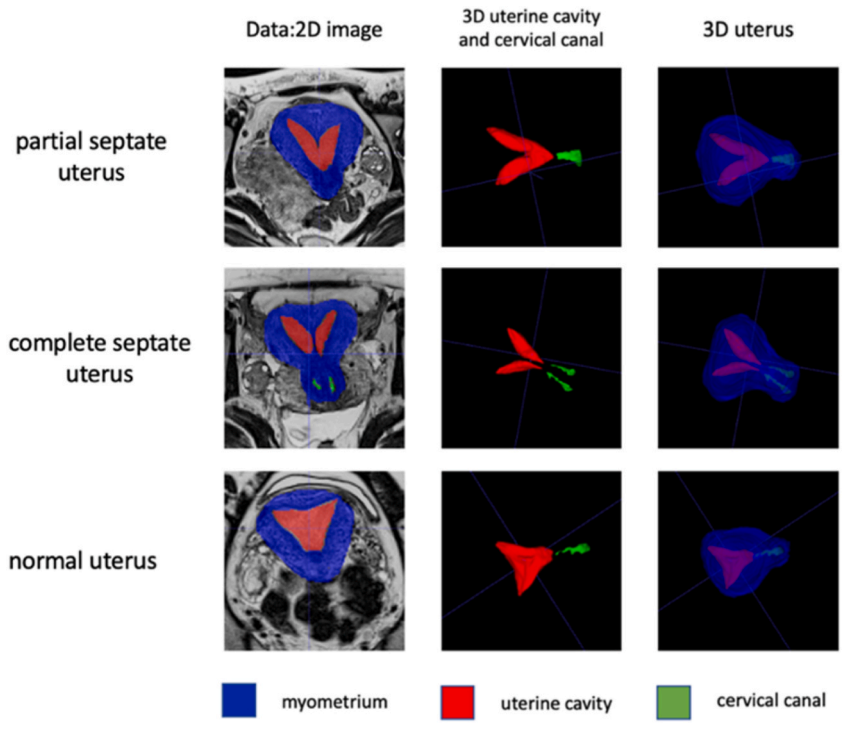

Fig. 1. Results of segmentation of the myometrium, uterine cavity, and cervical canal on axial view and in 3D reconstruction mode (best viewed in color).

L, the length of the long axis, varies from 36 to 104. Each image has its corresponding annotation $\mathbf{Y}$, which is a binary mask. $\mathbf{Y}$ has the same size as $\mathbf{X}$, with each voxel being either 0 or 1 (indicating the target).

Each 3D volume X is sliced along three axes—coronal, sagittal and axial—and these 2D slices are denoted by $\mathbf{X}_{C,\omega}(\omega = 1,2,...,W)$,$\mathbf{X}_{S,h}(h = 1,2,...,H)$ and $\mathbf{X}_{A,l}(l = 1,2,...,L)$, where the subscripts C, S, and A represent the coronal, sagittal, and axial views, respectively. For each view, we trained an individual 2D-FCN network, denoted by $\mathbf{M}_C$,$\mathbf{M}_S$, and $\mathbf{M}_A$. To incorporate contextual information, we input the image along with its three neighboring slices into the model. At the testing stage, we fused the segmentation results from the three axes to obtain higher accuracy. For the sake of simplicity, we use $\mathbf{X}_{A,l}$ to denote the original input image in the following paragraphs. The FCN outputs a probability map $\mathbf{P}_{A,l} = f[\mathbf{X}_{A,l};\boldsymbol{\theta}]$ with input $\mathbf{X}_{A,l}$, where $f[\cdot;\boldsymbol{\theta}]$ is a neural network (e.g., the FCN used in this paper) with $\boldsymbol{\theta}$ representing network parameters. $\mathbf{P}_{A,l}$ has the same size as $\mathbf{X}_{A,l}$, with each voxel ranging from [0, 1]. To obtain binary mask $\mathbf{Z}_{A,l}$, a fixed threshold of 0.5 was used, as is typical in deep learning, i.e., $\mathbf{Z}_{A,l} = \mathbf{1}[\mathbf{P}_{A,l} \geq 0.5]$.

2.4.2. Recurrent saliency transformation network

In the RSTN, we followed the coarse-to-fine pipeline, which has two training stages, namely, the coarse and fine stages, as shown in Fig. 2. At the coarse stage, we fed $\mathbf{X}_{A,l}$ into the model and then obtained the probability map $\mathbf{P}_{A,l}$. To make full use of $\mathbf{P}_{A,l}$, we introduced a saliency transformation module, which takes $\mathbf{P}_{A,l}$ and generates an image with spatial attention, i.e., $\mathbf{I}_{A,l} = \mathbf{X}_{A,l} \odot g[\mathbf{P}_{A,l};\eta]$. Here, $g[\cdot;\eta]$ is the transformation function parameterized by η, and $\odot$ denotes elementwise point. At the fine stage, $\mathbf{I}_{A,l}$ is fed into the model in place of $\mathbf{X}_{A,l}$. Given an input image $\mathbf{X}_{A,l}$ and integer T, which indicates the maximal number of training iterations, we update $\mathbf{I}_{A,l}^{(t)}$ and $\mathbf{P}_{A,l}^{(t)}$ periodically for $t = 0,1,...,T$ (1):

$$\mathbf{I}_{A,l}^{(t)} = \mathbf{X}_{A,l} \odot \mathbf{g}\left(\mathbf{P}_{A,l}^{(t-1)};\eta\right), \mathbf{P}_{A,l}^{(t)} = \mathrm{f}\left[\mathbf{I}_{A,l}^{(t)};\theta\right]. \tag{1}$$

Note that the original input image $\mathbf{X}_{A,l}$ remains unchanged, and the parameters $\boldsymbol{\theta}$ and η are shared by all iterations except for an individual $\boldsymbol{\theta}$ for $t = 0$. We simply start with $\mathbf{I}_{A,l}^{(0)} = \mathbf{X}_{A,l}$ for $t = 0$. We then define a cropping operation $\mathrm{Crop}[\cdot;\mathbf{P}_{A,l}^{(t)}]$; this operation takes $\mathbf{P}_{A,l}^{(t)}$ as a reference map, binarizes it into $\mathbf{Z}_{A,l}^{(t)} = \mathbf{1}[\mathbf{P}_{A,l}^{(t)} \geq 0.5]$ and computes the minimal 2D bounding box that contains all these pixels. It is also important to note that the size of the original input image $\mathbf{I}_{A,l}^{(0)}$ is different from $\mathbf{I}_{A,l}^{(t)}$. To avoid confusing the neural networks, we use two FCNs, called coarse-scaled and fine-scaled segmentation networks, to handle the original and cropped images. The former is used only in the first iteration $(t = 0)$, and the latter is responsible for the remaining iterations. $\boldsymbol{\theta}^C$ and $\boldsymbol{\theta}^F$ denote the parameters of the two networks, which were jointly optimized.

Models were optimized through the stochastic gradient method by the loss function; here, we apply DSC loss. The loss on $\mathbf{P}_{A,l}^{(t)}$, $t = 0,1,...,T$ is denoted by $\mathbf{L}\{\mathbf{Y}_{A,l},\mathbf{P}_{A,l}^{(t)}\}$. The overall loss function is as follows (2):

$$\mathbf{L} = \sum_{t=0}^{T} \lambda_t \cdot \mathbf{L}\left\{\mathbf{Y}_{A,l}^{(t)},\mathbf{Z}_{A,l}^{(t)}\right\} \tag{2}$$

where $\{\lambda_t\}_{t=0}^{T}$ indicates the tradeoff of the loss terms. We set $2\lambda_0 = \lambda_1 = ... = \lambda_T = 2/(2T+1)$ to encourage accurate, fine-scaled seg-

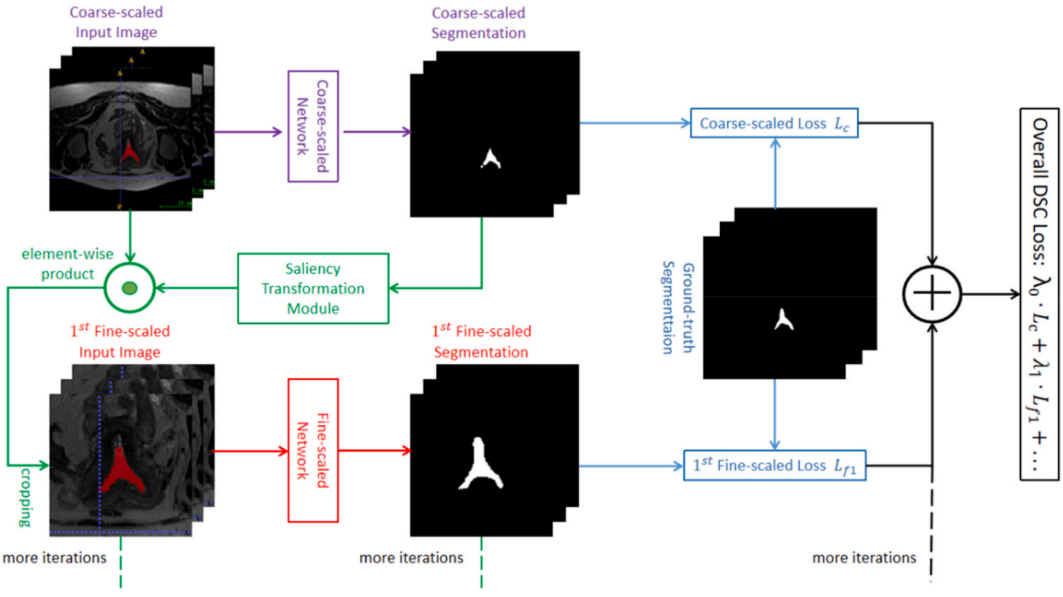

Fig. 2. Illustration of the RSTN. To save space, we only show the coarse stage and first iterations of the remaining stages.

mentation. This leads to a joint optimization of the FCN parameters θ^C and θ^F and transformation parameters η.

2.4.3. Validating the algorithm

We did not use a constant T as the maximum iteration. In practice, training iterations were continued until two consecutive predictions DSC$\{Z^{(t-1)},Z^{(t)}\}$ reached a given threshold τ. DSC$\{Z^{(t-1)},Z^{(t)}\}$ was computed as follows (3):

$$\mathrm{DSC}\left\{\mathbf{Z}^{(t-1)},\mathbf{Z}^{(t)}\right\}=\frac{2\times\sum_i\mathbf{Z}_i^{(t-1)}\mathbf{Z}_i^{(t)}}{\sum_i\mathbf{Z}_i^{(t-1)}+\mathbf{Z}_i^{(t)}} \tag{3}$$

We set four different similarity thresholds for τ: 90 %, 95 %, 98 %, and 99 %. When the iterations stopped, we computed the DSC score between the latest prediction $\mathbf{Z}_i$ and the manual segmentation $\mathbf{Y}_i$ (4):

$$\mathrm{DSC}\left\{\mathbf{Z}_i,\mathbf{Y}_i\right\}=\frac{2\times\sum_i\mathbf{Z}_i\mathbf{Y}_i}{\sum_i\mathbf{Z}_i+\mathbf{Y}_i} \tag{4}$$

3. Results

3.1. 3D shape feature data

All the shape features of the UC and UM were analyzed in the three groups: the control group (normal uterus, 27.44 ± 3.20 years old), the partial septate group (26.55 ± 2.87 years old), and the complete septate group (26.55 ± 2.87 years old) (Table 1). There were no significant differences in age, Elongation, LeastAxisLength, Maximum2DDiameterRow, MeshVolume, or SurfaceVolumeRatio between the three groups ($P > 0.05$). The values of four shape features (MajorAxisLength, Maximum2DDiameterColumn, MinorAxisLength, and SurfaceArea) were significantly lower in the UC of the control group than in that of the partial septate group and the complete septate group, while the values of two features (Flatness and Sphericity) were significantly higher ($p < 0.05$, Fig. 3). The UCs of the three groups significantly differed in both Flatness and Sphericity. The values of six shape features (Maximum2DDiameterSlice, Maximum3DDiameter, MeshVolume, MinorAxisLength, VoxelVolume and SurfaceArea) were significantly lower in the UMs of the control group than in those of the partial septate group and the complete septate group ($p < 0.05$, Fig. 4).

3.2. Deep learning data

In this section, we visualize the segmentation results at both the 2D and 3D levels, as shown in Figs. 5 and 6. As the results show, a higher threshold leads to a better result. The DSC scores of the four folds for different thresholds were all over 80 %. In addition to the DSC score (Table 2), we computed the volume ratio between predictions and manual segmentation (Table 3). The average ratio was 101.2 %, implying that the results of automatic segmentation would be meaningful in clinical practice.

4. Discussion

We sought to determine the differences in 3D shape features between SU and normal uterus based on 3D reconstruction. The values of six shape features of the UC significantly differed between the control group and the other two groups. The UCs of the three groups were significantly different in terms of flatness and sphericity. The values of six shape features were significantly lower in the UMs of the control group than in those of the partial septate group and the complete septate group. This may be because the septum increases

Table 1
p values of shape features in the three groups.

Shape Features (3D)	Normal vs. partial		Normal vs. complete		Partial vs. complete	
	UC	UM	UC	UM	UC	UM
Elongation	0.305	0.049	0.694	0.355	0.076	0.274
Flatness	<0.001	0.724	0.005	0.676	0.027	0.836
LeastAxisLength	0.004	0.700	0.968	0.558	0.091	0.790
MajorAxisLength	<0.001	0.171	0.001	0.049	0.466	0.310
Maximum2DDiameterColumn	0.007	0.291	0.038	0.553	0.312	0.593
Maximum2DDiameterRow	0.859	0.250	0.163	0.081	0.432	0.437
Maximum2DDiameterSlice	0.069	0.019	0.166	0.007	0.259	0.889
Maximum3DDiameter	0.030	0.009	0.296	0.011	0.060	0.769
MeshVolume	0.329	0.034	0.383	0.036	0.853	0.948
MinorAxisLength	0.004	0.009	0.001	0.039	0.133	0.569
Sphericity	<0.001	0.946	<0.001	0.065	0.001	0.014
SurfaceArea	0.011	0.042	0.011	0.011	0.459	0.447
SurfaceVolumeRatio	0.115	0.212	0.016	0.723	0.294	0.304
VoxelVolume	0.325	0.034	0.372	0.037	0.841	0.952

UC, uterine cavity; UM, uterine myometrium.

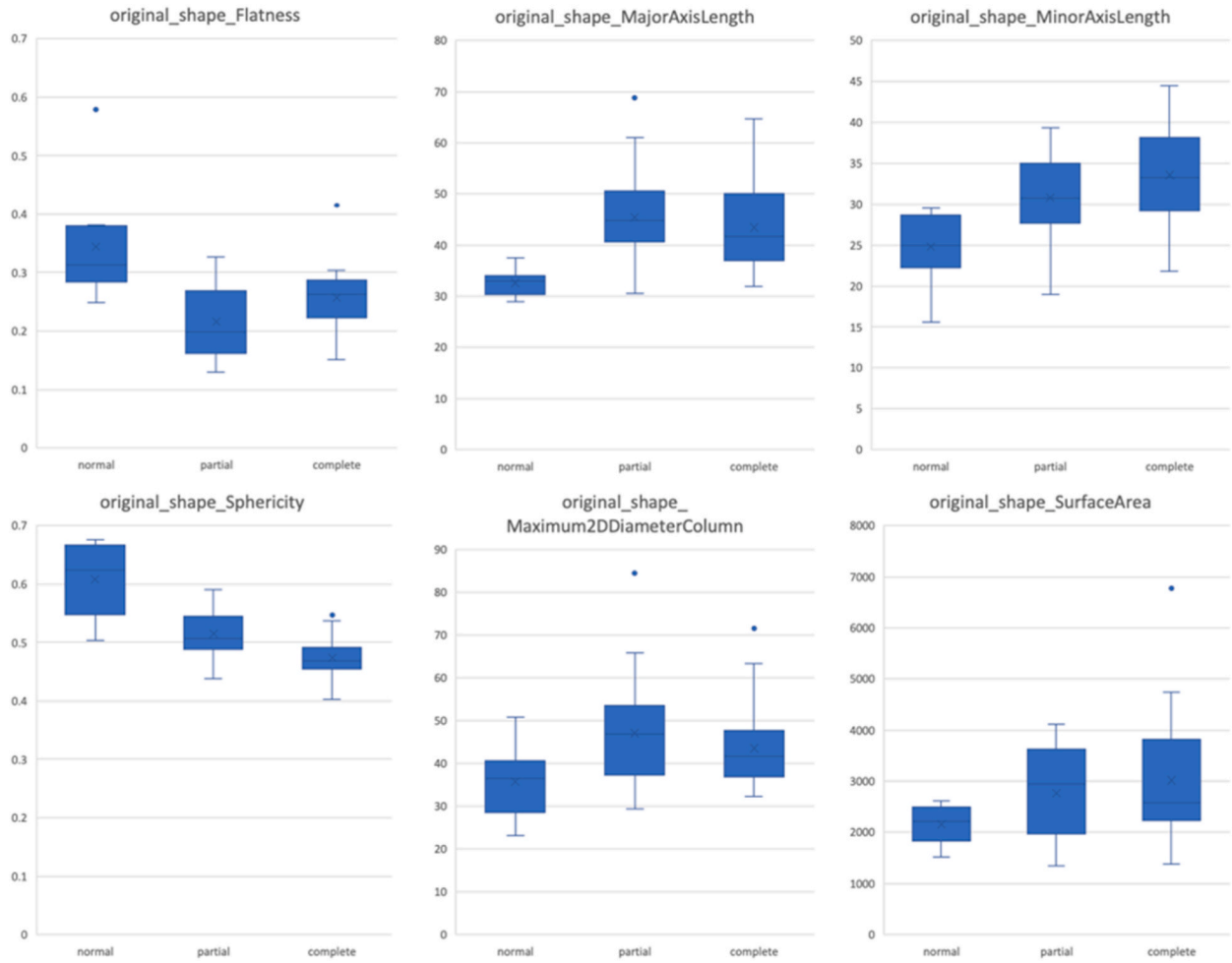

Fig. 3. Comparison of a subset of selected 3D shape features of the UC among the three groups. The x-axis represents groups, and the y-axis shows the feature values.

the complexity of the myometrium and UC morphology. The *p* values obtained for shape features of the UC were lower than those of the UM, which means that analyzing shape features of the UC might be more sensitive and valuable in future big-data analysis.

Using 3D shape features to analyze uterine morphology is more accurate than the traditional method of measuring endometrial thickness, UC major axis length, and UC volume. The traditional measurement method includes manual measurement of the endometrial thickness, UC length, and UC volume on the images by radiologists. This method is a time-consuming, laborious process and has a certain amount of error. This study used manual segmentation of the uterus and *PyRadiomics* software to extract 3D shape features. In addition to endometrial thickness (MinorAxisLength of UC), UC axis length (MajorAxisLength of UC), and UC volume (VoxelVolume of UC), other objective parameters are used for analysis.

Many researchers have investigated 3D reconstruction of the uterus. All these studies had two main aims: to diagnose disease more precisely [12] and to locate lesions correctly before surgery [13,14], In these studies, 3D reconstructions were based on images with a 2–4 mm slice thickness, and the accuracy values were not very high. Input images with higher resolution (smaller thickness and voxel size) will always produce 3D reconstruction masks with higher resolution, i.e., higher-precision 3D reconstruction. The 3D T2WI SPACE sequence we used in this study has a slice thickness of 1 mm and a voxel size of 1 $\times$ 1 $\times$ 1 mm, which not only enables MPR of the uterus on 2D images but also provides the possibility for higher-precision 3D reconstruction.

The reconstruction of vessels and nerves is based on the high signal of blood vessels and nerves in the image, which can be reconstructed by maximum intensity projection (MIP) [15,16]. However, the contrast between the signals of the uterus, most lesions, and the surrounding tissues is not very obvious, and reconstruction of the uterus can be performed only in the form of a manual sketch, which can take approximately 3 h. After machine learning is used to segment the UC automatically, it takes only a few seconds to reconstruct one case. This has greatly improved work efficiency and made future research with big data possible. In addition, automatic segmentation can produce 3D images with higher smoothness and accuracy, avoiding stepping artifacts during manual segmentation, which can be easily seen from the final 3D image.

Our segmentation framework is not specific to any particular body region but gives high-quality and robust results for segmenting

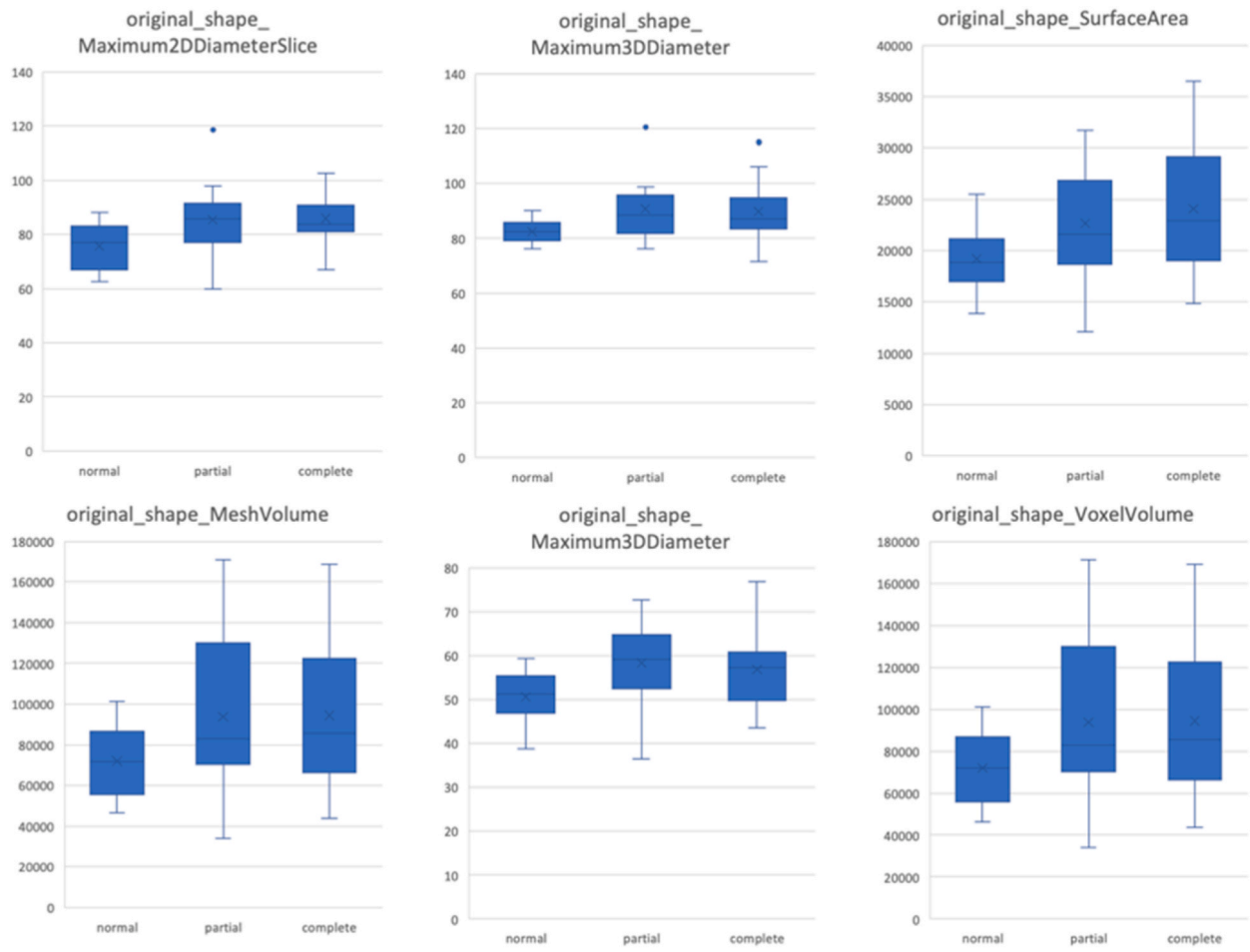

Fig. 4. Comparison of a subset of selected 3D shape features of the UM among the three groups. The x-axis represents groups, and the y-axis shows the feature values.

the uterus, which is a challenging task due to the low contrast and large interindividual variations of this organ. The segmentation model employed in our work is an end-to-end coarse-to-fine segmentation network [11] that uses prediction from the first (coarse) stage to shrink the input region for the second (fine) stage. The network is very suitable for small organs, as the target can occupy only a small part of the input data and still be segmented accurately. Popular deep segmentation networks such as FCN [17] and DeepLab [18] can be easily confused by cluttered backgrounds. Benefiting from the network structure, the predicted mask from the fine stage has a fine contour, and the reconstructed shape is in accordance with the ground truth, i.e., the 3D reconstructions can clearly show normal uteri, complete septate uteri, and partial septate uteri. Although we used only 33 cases for training, we still achieved high performance, with Dice coefficients of 80 %–81 %, thanks to the data augmentation strategy. We expect that with more training data, the performance can be further improved.

There were some limitations to this study. Manual segmentation required a great deal of time, approximately 3 h for one case. When the automatic segmentation experiment achieved satisfactory results, we stopped manual segmentation and used only this portion of the data for this experiment. This resulted in a relatively small final dataset. In addition, the clinical data still need to be improved by assessing variables such as adverse pregnancy history and comparing UC volume before and after surgery. These improvements will be made in subsequent studies.

5. Conclusion

Based on 3D reconstruction, septate uterus can be comprehensively evaluated using 3D shape features, providing a reference for subsequent research. The uterine cavity can be automatically segmented on 3D MRI using the RSTN method.

Ethics statement

This study was reviewed and approved by the ethics committee of the Obstetrics and Gynecology Hospital of Fudan University, with

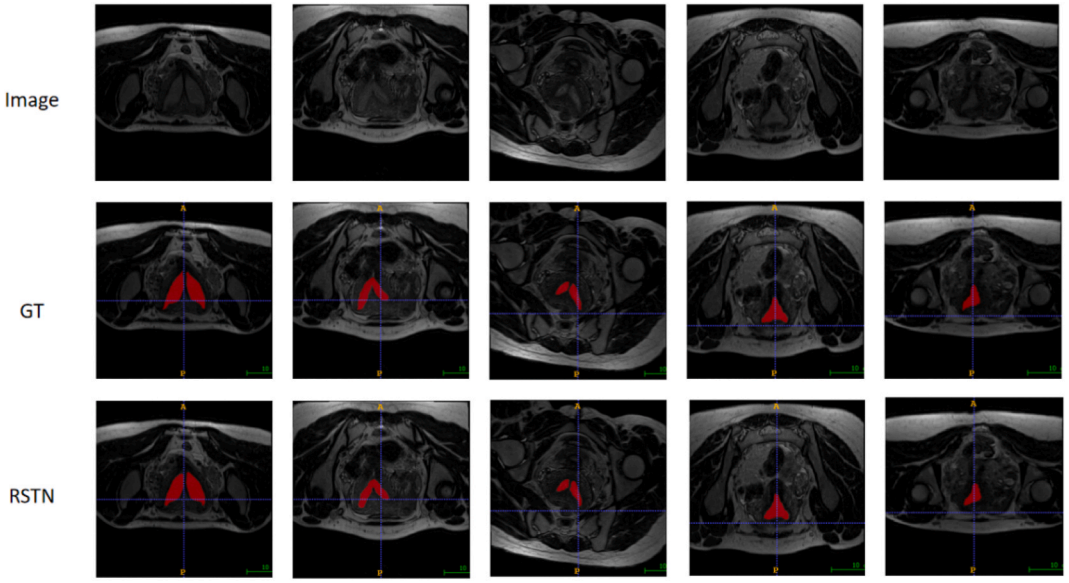

Fig. 5. A direct visual comparison between automatic (RSTN) and manual (GT) segmentation of nonreconstructed 2D images of various UC morphologies.

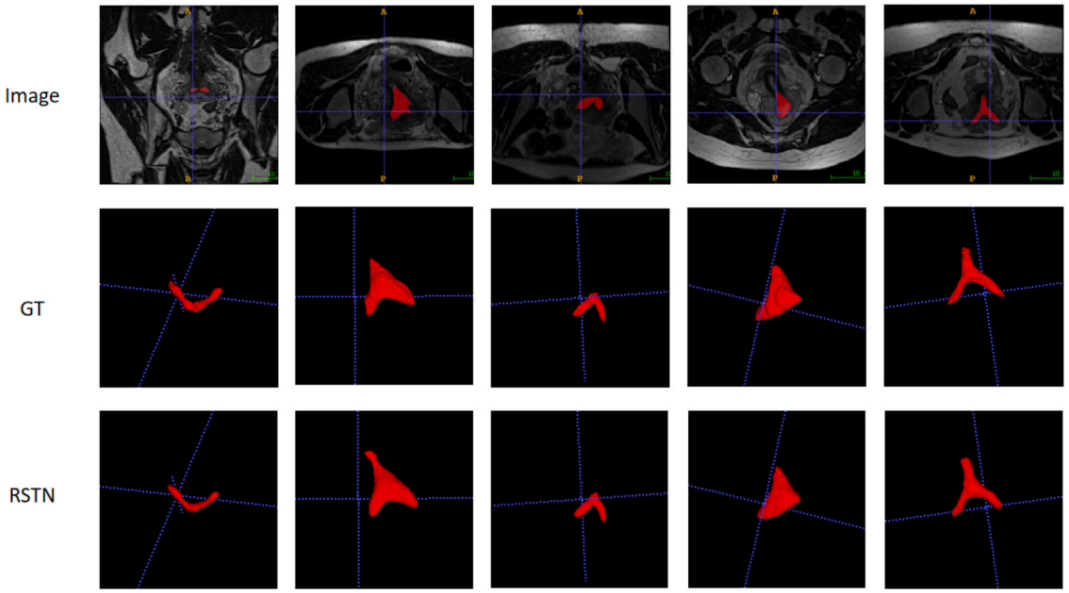

Fig. 6. A direct visual comparison between automatic (RSTN) and manual (GT) segmentation of 3D images of various UC morphologies. The automatically segmented UC morphologies were consistent with the manual segmentations but had a higher degree of smoothness.

Table 2
DSC scores of the four folds for different thresholds.

τ	Fold				
	0	1	2	3	Average
90 %	70.54 %	83.51 %	84.16 %	82.71 %	80.23 %
95 %	71.53 %	83.52 %	84.20 %	82.64 %	80.47 %
98 %	71.90 %	83.71 %	83.83 %	82.58 %	80.50 %
99 %	71.78 %	83.80 %	86.63 %	82.60 %	81.20 %

Table 3
Volume ratio between prediction and manual segmentation.

	Fold 0	Fold 1	Fold 2	Fold 3	Average
Volume ratio(Z/Y)	78.20 %	96.20 %	115.10 %	115.20 %	101.20 %

approval number: 2022-77.

All participants/patients provided informed consent to participate in the study.

All participants/patients provided informed consent for the publication of their anonymized case details and images.

Data availability statement

Data has not been deposited into a publicly available repository but will be made available on request.

Additional information

No additional information is available for this paper.

CRediT authorship contribution statement

Qing Zhou: Writing - original draft, Investigation, Data curation, Conceptualization. **Yunhao Bai:** Writing - original draft, Investigation, Data curation. **Fang Chen:** Writing - original draft, Investigation, Data curation. **He Zhang:** Resources, Formal analysis. **Limei Chen:** Resources, Methodology. **Guofu Zhang:** Writing - review & editing, Supervision, Resources. **Yan Wang:** Writing - review & editing, Supervision, Data curation, Conceptualization. **Long Sui:** Writing - review & editing, Resources, Project administration, Funding acquisition, Conceptualization.

Declaration of competing interest

The authors declare the following financial interests/personal relationships which may be considered as potential competing interests:Long Sui reports financial support was provided by National Science Foundation of Shanghai, China 22ZR1408800.

References

[1] J.M. Turocy, B.W. Rackow, Uterine factor in recurrent pregnancy loss, Semin. Perinatol. 43 (2019) 74–79, https://doi.org/10.1053/j.semperi.2018.12.003.
[2] G.F. Grimbizis, S. Gordts, A. Di Spiezio Sardo, S. Brucker, C. De Angelis, M. Gergolet, et al., The ESHRE-ESGE consensus on the classification of female genital tract congenital anomalies, Gynecol. Surg. 10 (2013) 199–212, https://doi.org/10.1007/s10397-013-0800-x.
[3] Y.Y. Chan, K. Jayaprakasan, J. Zamora, J.G. Thornton, N. Raine-Fenning, A. Coomarasamy, The prevalence of congenital uterine anomalies in unselected and high-risk populations: a systematic review, Hum. Reprod. Update 17 (2011) 761–771, https://doi.org/10.1093/humupd/dmr028.
[4] P. Medicine, Practice committee of the American society for reproductive medicine. Uterine septum: a guideline, Fertil. Steril. 106 (3) (2016) 530–540, https://doi.org/10.1016/j.fertnstert.2016.05.014.
[5] C.A. Venetis, S.P. Papadopoulos, R. Campo, S. Gordts, B.C. Tarlatzis, G.F. Grimbizis, Clinical implications of congenital uterine anomalies: a meta-analysis of comparative studies, Reprod. Biomed. Online 29 (2014) 665–683, https://doi.org/10.1016/j.rbmo.2014.09.006.
[6] J.F.W. Rikken, C.R. Kowalik, M.H. Emanuel, M.Y. Bongers, T. Spinder, F.W. Jansen, et al., Septum resection versus expectant management in women with a septate uterus: an international multicentre open-label randomized controlled trial, Hum. Reprod. 36 (2021) 1260–1267, https://doi.org/10.1093/humrep/deab037.
[7] Z. Wang, J. An, Y. Su, C. Liu, S. Lin, J. Zhang, X. Xie, Reproductive outcome of a complete septate uterus after hysteroscopic metroplasty, J. Int. Med. Res. 48 (2020), 300060519893836, https://doi.org/10.1177/0300060519893836.
[8] Practice Committee of the American Society for Reproductive Medicine, Electronic address aao and M practice committee of the American society for reproductive. Uterine septum: a guideline, Fertil. Steril. 106 (2016) 530–540, https://doi.org/10.1016/j.fertnstert.2016.05.014.
[9] C. Maciel, N. Bharwani, R.A. Kubik-Huch, L. Manganaro, M. Otero-Garcia, S. Nougaret, et al., MRI of female genital tract congenital anomalies: European Society of Urogenital Radiology (ESUR) guidelines, Eur. Radiol. 30 (2020) 4272–4283, https://doi.org/10.1007/s00330-020-06750-8.
[10] S.C. Behr, J.L. Courtier, A. Qayyum, Imaging of mullerian duct anomalies, Radiographics 32 (2012) E233–E250, https://doi.org/10.1148/rg.326125515.
[11] L. Xie, Q. Yu, Y. Zhou, Y. Wang, E.K. Fishman, Yuille AL, Recurrent saliency transformation network for tiny target segmentation in abdominal CT scans, IEEE Trans. Med. Imag. 39 (2020) 514–525.
[12] H.X. Pan, P. Liu, H. Duan, P.F. Li, R.L. Chen, L. Tang, et al., Using 3D MRI can potentially enhance the ability of trained surgeons to more precisely diagnose Mullerian duct anomalies compared to MR alone, Eur. J. Obstet. Gynecol. Reprod. Biol. 228 (2018) 313–318, https://doi.org/10.1016/j.ejogrb.2018.07.007.
[13] S.R. Lee, Y.J. Kim, K.G. Kim, A fast 3-dimensional magnetic resonance imaging reconstruction for surgical planning of uterine myomectomy, J. Kor. Med. Sci. 33 (2018) e12, https://doi.org/10.3346/jkms.2018.33.e12.
[14] C.M. Durnea, S. Siddiqi, D. Nazarian, G. Munneke, P.M. Sedgwick, S.K. Doumouchtsis, 3D-Volume rendering of the pelvis with emphasis on paraurethral structures based on MRI scans and comparisons between 3D slicer and OsiriX(R), J. Med. Syst. 45 (2021) 27, https://doi.org/10.1007/s10916-020-01695-3.
[15] P. Li, P. Liu, C. Chen, H. Duan, W. Qiao, Ognami Oh, The 3D reconstructions of female pelvic autonomic nerves and their related organs based on MRI: a first step towards neuronavigation during nerve-sparing radical hysterectomy, Eur. Radiol. 28 (2018) 4561–4569, https://doi.org/10.1007/s00330-018-5453-8.
[16] C. Huynh, T.N. Ha, V.T. Hoang, P.H. Huynh, Acquired life-threatening uterine arteriovenous malformation treated by endovascular embolization, Radiol Case Rep 16 (2021) 241–245, https://doi.org/10.1016/j.radcr.2020.11.013.
[17] E. Shelhamer, J. Long, T. Darrell, Fully convolutional networks for semantic segmentation, IEEE Trans. Pattern Anal. Mach. Intell. 39 (2017) 640–651, https://doi.org/10.1109/TPAMI.2016.2572683.
[18] L.C. Chen, G. Papandreou, I. Kokkinos, K. Murphy, Yuille AL, DeepLab: semantic image segmentation with deep convolutional nets, atrous convolution, and fully connected CRFs, IEEE Trans. Pattern Anal. Mach. Intell. 40 (2018) 834–848, https://doi.org/10.1109/TPAMI.2017.2699184.